Supermassive black hole binaries in gaseous and stellar circumnuclear discs: orbital dynamics and gas accretion.

M. Dotti¹, M. Colpi², F. Haardt¹, & L. Mayer^{3,4}

- Dipartimento di Fisica e Matematica, Università dell'Insubria, Via Valleggio 11, 22100 Como, Italy
- ² Dipartimento di Fisica G. Occhialini, Università degli Studi di Milano Bicocca, Piazza della Scienza 3, 20126 Milano, Italy
- ³ Institute for Theoretical Physics, University of Zurich, CH-8057, Zurich, Switzerland
- ⁴ Institute of Astronomy, Department of Physics, ETH, Zurich, Wolfgang-Pauli Strasse, CH-8095 Zurich, Switzerland

31 March 2018

ABSTRACT

The dynamics of two massive black holes in a rotationally supported nuclear disc of mass $M_{\rm disc} = 10^8 {\rm M}_{\odot}$ is explored using N-Body/SPH simulations. Gas and star particles are co-present in the disc. Described by a Mestel profile, the disc has a vertical support provided by turbulence of the gas, and by stellar velocity dispersion. A primary black hole of mass $4 \times 10^6 {\rm M}_{\odot}$ is placed at the centre of the disc, while a secondary black hole is set initially on an eccentric co-rotating orbit in the disc plane. Its mass is in a 1 to 1, 1 to 4, and 1 to 10 ratio, relative to the primary. With this choice, we mimic the dynamics of black hole pairs released in the nuclear region at the end of a gas-rich galaxy merger. It is found that, under the action of dynamical friction, the two black holes form a close binary in ~ 10 Myrs. The inspiral process is insensitive to the mass fraction in stars and gas present in the disc and is accompanied by the circularization of the orbit. We detail the gaseous mass profile bound to each black hole that can lead to the formation of two small Keplerian discs, weighing $\approx 2\%$ of the black hole mass, and of size ~ 0.01 pc. The mass of the tightly (loosely) bound particles increases (decreases) with time as the black holes spiral into closer and closer orbits. Double AGN activity is expected to occur on an estimated timescale of $\lesssim 10$ Myrs, comparable to the inspiral timescale. The double nuclear point-like sources that may appear during dynamical evolution will have typical separations of $\lesssim 10$ pc.

Key words: black hole physics – hydrodynamics – galaxies: starburst – galaxies: evolution – galaxies: nuclei

1 INTRODUCTION

Collisions of spiral galaxies may lead to the formation of (ultra-)luminous infrared galaxies (U-LIRGs). A clear example is NGC 6240, a ULIRG composed of two gas-rich galaxies on the verge of merging, hosting two spatially distinct X-ray sources. Buried in a wide-spread star burst, these two hard X-ray sources have been identified as a pair of accreting massive black holes (MBHs) (Komossa et al. 2003; Risaliti et al. 2006).

The majority of (U–)LIRGs are unsettled remnants of colliding galaxies undergoing episodes of intense star formation (see for a review Sanders & Mirabel 1996). A large number of (U–)LIRGs hosts a central rotationally supported massive gaseous disc (up to $10^{10} \rm M_{\odot}$) extending on scales of ~ 100 pc (Sanders & Mirabel 1996; Scoville, Yun & Bryant 1997; Downes & Solomon 1998; Tacconi et al. 1999; Bryant & Scoville 1999; Greve et al. 2006). As shown in numerical simulations, these discs may be the end–product

of gas-dynamical and gravitational torques (excited during the merger), driving large amounts of gas in the core of the remnant, where the MBHs are expected to reside (Barnes & Hernquist 1991, 1996; Kazantzidis et al. 2005). Inside these massive self-gravitating discs, MBH pairs continue their dynamical evolution, and can accrete gas.

The formation and evolution of MBH pairs in merging galaxies have a large number of potentially interesting astrophysical consequences. In gas—rich mergers, MBH binaries can produce, beside double active nuclei, other peculiar features such as periodic modulations (as seen in OJ 287), and wiggling jets (see Komossa 2006 for a review). In dry mergers, binary MBHs can erode the inner stellar cusp (Milosavljevic et al. 2002), creating a population of hypervelocity stars in galactic halos (Yu & Tremaine 2003; Brown et al. 2006). Ultimately, binary MBHs may eventually coalesce emitting low—frequency gravitational waves detectable

by LISA (Bender et al. 1994; Hughes 2002; Sesana et al. 2005).

Mayer et al. (2006) have shown that in dissipative mergers, large-scale inflows ending in the formation of massive turbulent nuclear discs facilitate the pairing of the MBHs hosted in the parent galaxies, and that an eccentric Keplerian binary forms. In this paper, we will explore the phase following the formation of the binary. In a previous work (Dotti, Colpi & Haardt 2006, hereafter DCH06), we studied the dynamical evolution of MBH pairs orbiting inside a massive gaseous disc (see also Escala et al. 2005), exploring different MBH mass ratios and initial orbital eccentricities. We showed that, during MBH inspiral, gas-dynamical frictional forces circularize the orbits (if initially corotating with the disc), and only after circularization a sizable amount of gas is captured by each MBH. The force resolution in such early simulations was not sufficient to resolve the small accretion discs that form around the inspiralling MBHs.

In the simulations presented in DCH06, the gaseous disc was embedded into a larger scale, spherically symmetric stellar distribution. Fragmentation of the disc was prevented by using an adiabatic equation of state, and star formation was, simply, neglected. Thus, these simulations did not consider the possible co-presence of an axisymmetric nuclear stellar disc. Indeed, nuclear stellar discs are observed in many early and late type galaxies (van den Bosch et al. 1998; Scorza & van den Bosch 1998; Morelli et al. 2004; Krajnovic & Jaffe 2004; Lopes et al. 2006; Mueller Sanchez et al. 2006; Davies et al. 2007). Nuclear stellar discs result from galaxy mergers and/or from the secular evolution of bars (Krajnovic & Jaffe 2004; Kormendy et al. 2005; Ferrarese et al. 2006). Davies et al. (2007), observing young stellar discs in NGC 1068 and NGC 1097, estimate masses of $\sim 10^8 {\rm M}_{\odot}$, radii of ~ 50 pc, and a vertical scale heights of $\sim 5-10$ pc, suggesting that the star velocity dispersion provides significant pressure support.

Aiming at a better understanding of i) the role of a nuclear stellar disc in driving the orbital evolution of the MBH binary, and ii) the formation of an accretion disc around each MBH, we run a new series of simulations employing the particle splitting technique (Kitsionas & Whitworth 2002), allowing us to improve the numerical resolution with respect to DCH06 and other similar simulations (Kazantzidis et al. 2005). In the most accurate simulation, we can resolve, on sub–parsec scales, the gravitational sphere of influence of each MBH. For the first time, we detail the mass profile of the gas bound to the MBHs, so that we can conjecture on the accretion process during the MBH pairing and inspiral.

The paper is organized as follows. In Section 2 we describe the equilibrium structure of the gaseous and stellar disc, and the initial conditions for our different runs. In Section 3 we present the results of our simulations carried on varying the MBH masses and the stellar content in the disc, as well as the aforementioned simulation at higher resolution, and finally, in Section 4 we draw our conclusions.

2 SIMULATION SETUP

We follow the dynamics of MBH pairs in nuclear discs using numerical simulations run with the N–Body/SPH code GADGET (Springel, Yoshida & White 2001).

In our models, a primary MBH of mass M_1 is placed at the centre of a gaseous and/or stellar disc, embedded in a larger scale stellar spheroid. A secondary MBH of mass M_2 is placed on a bound orbit in the disc plane.

The gaseous disc is modeled with 235331 particles, has a total mass $M_{\rm Disc}=10^8{\rm M}_\odot$, and follows a Mestel surface density profile

$$\Sigma(R) = \Sigma_0 \left(\frac{R_0}{R}\right),\tag{1}$$

where R is the radial distance projected into the disc plane, and Σ_0 is the density at scale radius R_0 . Fig. 1 shows the profile $\Sigma(R)$, in physical units. The disc is rotationally supported in R, has a finite radial extension of 100 pc, and finite vertical thickness of 10 pc. Initially, the gaseous particles are distributed uniformly along the vertical axis. The SPH particles evolve adiabatically, and the initial internal energy density profile scales as:

$$u(R) = KR^{-2/3}, (2)$$

where K is a constant defined so that the Toomre parameter of the disc,

$$Q = \frac{\kappa c_{\rm s}}{\pi G \Sigma},\tag{3}$$

is > 3 everywhere, preventing disc fragmentation and formation of large scale over–densities, such as bars and spiral arms. In equation (3) κ is the local epicyclic frequency, and $c_{\rm s}$ the local sound speed of the gas, that, for our choice of K, is $\approx 30\,{\rm km\,s^{-1}}$ at R=50 pc. The internal energy of gas particles mimics the internal, unresolved turbulence, and, as a consequence, $c_{\rm s}$ has to be considered as the local turbulent velocity.

The spheroidal component (bulge) is modeled with 10^5 collisionless particles, initially distributed as a Plummer sphere with mass density profile (shown in Fig. 2)

$$\rho(r) = \frac{3}{4\pi} \frac{M_{\text{Bulge}}}{b^3} \left(1 + \frac{r^2}{b^2} \right)^{-5/2},\tag{4}$$

where b = 50 pc is the core radius, r the radial coordinate, and $M_{\rm Bulge} = 6.98 M_{\rm Disc}$ the total mass of the spheroid. With such choice, the mass of the bulge within 100 pc is 5 times the mass of the disc, as suggested by Downes & Solomon (1998).

The primary MBH has a mass $M_1 = 4 \times 10^6 \,\mathrm{M}_{\odot}$, while for the secondary we consider three different values, equal to $4 \times 10^5 \,\mathrm{M}_{\odot}$, $10^6 \,\mathrm{M}_{\odot}$ and $4 \times 10^6 \,\mathrm{M}_{\odot}$, respectively. The secondary MBH is placed inside the massive disc on an eccentric orbit with eccentricity $e \simeq 0.7$, at a separation of 50 pc from the central MBH.

We evolve our initial composite model (bulge, disc and primary MBH) for ≈ 3 Myrs, until the bulge and the disc reach equilibrium. Given the initial homogeneous vertical structure of the disc, the gas initially collapses on the disc plane exciting small waves that propagate through the system. The spheroid is gravitationally stable on large scales $(r \gtrsim 20~{\rm pc})$ and contracts in the central region until equilibrium is reached. Fig. 1 and 2 show the equilibrium profiles, and in particular the density enhancement in the central region of the spheroid. The stellar density increase does not affect the inner region $(r \lesssim 10~{\rm pc})$ of the (denser) disc nor the dynamics of the MBHs.

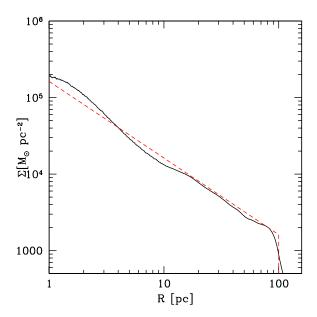


Figure 1. Gaseous disc surface density Σ as a function of distance R from the central MBH. Red dashed line refers to the surface density of the Mestel disc (i.e., the disc before it reaches equilibrium), while black solid line describes the equilibrium profile after an elapsed time ≈ 3 Myrs.

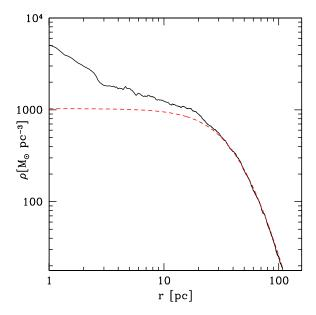


Figure 2. Density ρ of the stellar spheroid as a function of distance r form the central MBH. Red dashed line refers to the initial Plummer profile, while black solid line refers to the equilibrium profile

We run four different sets of simulations (for a total of 12 according to the mass M_2 of the secondary MBH), assuming a purely gaseous disc, and a disc in which 1/3, 2/3, and, finally, all gas particles are turned into collisionless particles, respectively. For each disc model with fixed star fraction, we evolved the initial condition in isolation until equilibrium is reached, as indicated above. The gas \rightarrow star conversion in the disc is obtained converting randomly selected gas particles in collisionless particles. The latter own the same mass and position of the initial gas particles, so that the stellar disc component follows the same density distribution of the gas. The velocities of the transformed particles are modified by adding an isotropic component equal (in modulus) to the local sound speed, preventing the vertical collapse of the new disc. Gas particles are transformed at a constant rate of $\approx 160 \, \rm M_{\odot} yr^{-1}$. This rate prevents spurious relaxation that could, in principle, change the structure of the disc. The outputs of this trial simulation at three different times (t \approx 0.2, 0.4, and 0.6 Myrs) correspond to a fraction of 1/3, 2/3, and to the total disc mass transformed in stars. These outputs are used as new initial conditions for the three sets of simulations with an axisymmetric stellar population. We do not convert any gaseous particle in stars when we follow the dynamics of the MBHs, so that the disc stellar fraction remains constant. The secondary MBH is inserted in the plane of the disc, after the composite system has relaxed to equilibrium.

The number of particles used to model the two components allows for a spatial resolution $\simeq 1$ pc, corresponding to the gravitational softening which is the same for the collisionless, gaseous and MBH particles. The thermodynamical parameters of the gaseous disc are evaluated averaging over a subsample of 50 neighbours.

The mass of the primary and the mass ratio $q=M_2/M_1$ fix two characteristic scale–lengths. Following Merritt (2006), we define the gravitational influence radius of the larger MBH $(r_{\rm inf})$ as the radius of a sphere that encloses a mass (in gas and stars) equal to $2M_1$. For separations smaller than $r_{\rm inf}$ the two MBHs form a "binary". For the Plummer sphere and Mestel disc parameters used, $r_{\rm inf}\approx 6$ pc, so it is well resolved in our simulations. When the binary forms, we can estimate the hardening radius $a_{\rm h}$. Assuming a SIS profile, $a_{\rm h}=0.25\,q\,r_{\rm inf}/(1-q)^2$ (Merritt 2006), and, for $q=1,\,a_{\rm h}\approx 1$ pc, while for q=0.25 (0.1) $a_{\rm h}\approx 0.3$ (0.1) pc.

The main input parameters of our simulations are summarized in Table 1. We also performed a simulation at higher resolution, starting from an intermediate snapshot of run A1, that will be detailed and discussed in section 3.2.

3 RESULTS

3.1 Orbital decay and circularization

Fig. 3 shows the MBH relative separation s and eccentricity as a function of time (upper and lower panel respectively) for equal mass binaries (runs A1, B1, C1, and D1). Regardless the fraction of star–to–gas disc particles, the secondary MBH spirals in at the same pace, reaching the force resolution limit of ~ 1 pc after ~ 5 Myrs. The velocity dispersion of stars is similar to the gas sound speed, and the two components share the same differential rotation. This is why the

Table 1. Run parameters

run	f_*^a	M_1^b	M_2^b	$M_{ m Disc}^b$	$M_{ m Bulge}^b$, e
A1 ^c A2 A3		4	4 1 0.4	100	698	0.7
B1 B2 B3	1/3	4	4 1 0.4	100	698	0.7
C1 C2 C3	2/3		4 1 0.4	100	698	0.7
D1 D2 D3	1	4	4 1 0.4	100	698	0.7

^a f_* : disc mass fraction in stars.

^c Simulation A1 was run also using the particle splitting technique to improve force resolution (down to $\simeq 0.1$ pc, see sect. 3.2).

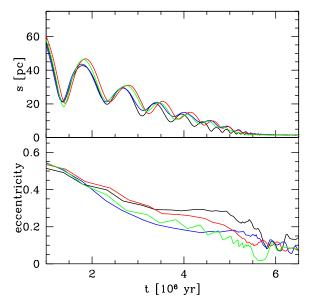


Figure 3. Equal mass MBHs. Upper panel: separations s (pc) between the MBHs as a function of time. Lower panel: eccentricity of the MBH binary as a function of time. Black, blue, red and green lines refer to stellar to total disc mass ratio of 0, 1/3, 2/3 and 1 (run A1, B1, C1, and D1) respectively.

dynamical friction on M_2 caused by stars and gas is similar. As the orbit decays, the eccentricity decreases to $e \leq 0.2$. This value is not a physical lower limit, but rather a numerical artifact due to the finite resolution. Circularization was found in DCH06 for a full gaseous disc. Here, we show that circularization occurs regardless the nature of the disc particles (gas and/or stars). Note that circularization takes place well before the secondary feels the gravitational potential of M_1 , so the MBH mass ratio does not play any role in the process.

To show how the circularization process works, consider run C1, where both stellar and gaseous particles are present in the disc. In Fig. 4 we plot the gas (left panels) and stellar (right panels) densities in the disc at two different times, corresponding to the first passage at pericentre (upper panels), and at apocentre (lower panels). The green curve shows the counterclockwise corotating orbit of the secondary MBH. Near to pericentre, the MBH has a velocity larger than the local rotational velocity, so that dynamical friction causes a reduction of the velocity of the MBH. A wake of particles lags behind the MBH trail. On the other hand, near to apocentre, the MBH velocity (mainly tangential) is lower than the disc rotational velocity, and, in this case, the force increases the MBH angular momentum: the wake is dragged in front of the MBH trail. Thus, as a result of differential rotation, the wake reverses its direction at apocentre accelerating tangentially the MBH, leading to circularization of M_2 orbit (see also Fig. 3). This seems a generic feature, regardless the disc composition, as long as the rotational velocity exceeds the gas sound speed and the stellar velocity dispersion, as in all cases explored. We remark that in spherical backgrounds, dynamical friction tends to increase the eccentricity, both in collisionless (Colpi, Mayer & Governato 1999; van den Bosch et al. 1999; Arena & Bertin 2007) and in gaseous (Sanchez-Salcedo & Brandenburg 2001) environments.

Fig. 5 shows the MBH separation and eccentricity evolution for the cases with $M_2 = 10^6 \,\mathrm{M}_{\odot}$ (runs "2" for all sets). The color coding is the same as in Fig. 3. As the dynamical friction time-scale is $\propto 1/M_2$ (for given disc properties), in this case M_2 orbital decay occurs on a time ≈ 4 longer than in runs "1". We can also observe that, in the case of a pure gaseous disc (run A2), circularization is more efficient compared to all other runs. When the secondary MBH moves along the eccentric orbit, its motion is supersonic for nearly all the entire orbit. Since for a supersonic perturber in a gaseous background dynamical friction is ≈ 2 times more efficient that in a stellar environment (Ostriker 1999), the circularization efficiency is increased (while, as discussed above, the orbital decay time-scale is nearly independent on the nature of the disc particles).

The same scalings hold for runs "3", where M_2 = $4 \times 10^5 \,\mathrm{M}_{\odot}$. The differences in the orbital decay timescale among runs A3, B3, C3 and D3, are however larger than what found in runs "1" and "2", because of the smaller secondary-to-background particles mass ratio. In runs "3" a random component of the motion of M_2 exists, mainly caused by the stellar bulge. In fact, the mass ratio between M_2 and a single bulge particle is 57, so that the background can not be treated as a smooth fluid.

^b Masses are in units of $10^6 \,\mathrm{M}_{\odot}$.

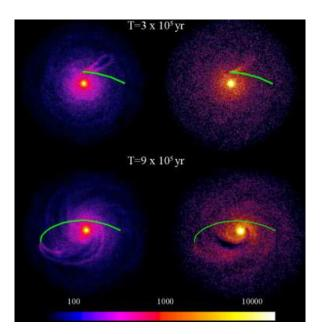


Figure 4. Snapshots from run C1. The panels show a face—on projection of the disc and MBH positions at two different times. The color coding indicates the z–averaged gas density (left panel) and star density (right panel) in logarithmic scale (units: M_{\odot}/pc^3). The green line traces the MBH counterclockwise prograde orbit. The gaseous (stellar) disc radius is $R \approx 100$ pc.

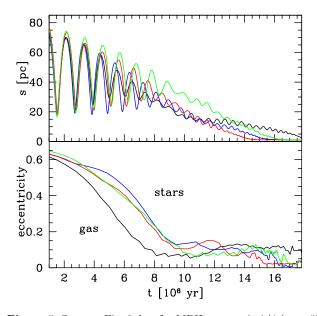


Figure 5. Same as Fig. 3, but for MBH mass ratio 1/4 (runs "2" in all sets). Upper panel: separations s (pc) between the MBHs as a function of time. Lower panel: eccentricity as a function of time. Black, blue, red and green lines refer to stellar to total disc mass ratio of 0, 1/3, 2/3 and 1 (run A2, B2, C2, and D2), respectively.

3.2 Nuclear discs around the spiraling MBHs: the high resolution run

We run a higher resolution simulation to study the eccentricity and orbital evolution on scales lower than 1 pc. The new initial condition is obtained resampling the output of run A1 (for equal mass MBHs) with the technique of particle splitting. Resampling is performed when the MBH separation is $\simeq 14$ pc (corresponding to $\simeq 4$ Myrs after the start of the simulation). We split each gas particle into $N_{\rm ch} = 10$ "child" particles (Kitsionas & Whitworth 2002), randomly distributed around the position of the original parent particle within a volume of size $\sim h_{\rm p}^3$, where $h_{\rm p}$ is the gravitational softening (of the parent particles). The velocities and temperatures of the child particles are set equal to that of the parent ones. Each child particle has a mass equal to $1/N_{\rm ch}$ of the mass of the parent. Splitting is applied to all particles whose distance from the binary centre of mass is ≤ 42 pc, so that the total number of particles increases only by a factor \simeq 4, while the local mass resolution in the split region is comparable to that of a standard $\simeq 2 \times 10^6$ particle simulation with uniform resolution. Our choice of the maximum distance for splitting is conservative, aimed at preventing that more massive, unsplit gas particles reach the binary on a timescale shorter than the entire simulation time. In the central split region, the high mass resolution achieved fulfills the Bate & Burkert (1997) criterion for gravitational softening values down to 0.1 pc. In other words, the resolution scales of hydrodynamical forces (SPH smoothing) and gravitational forces (gravitational softening) are similar. In particular, a sphere with radius ≈ 0.1 pc (corresponding to the new gravitational softening) centred on a particle contains $\gtrsim 1$ SPH kernel ($N_{\text{neigh}} = 50$ particles for our simulations). In Fig. 6 we compare the surface density profile of the circum-nuclear gaseous disc in run A1 at t = 4 Myrs, for the low and high resolution cases. The two profiles differ only below the scale of the low resolution limit $R \lesssim 3$ pc. The decrease of the gravitational softening corresponds to introducing a deeper potential well of the MBH within a sphere defined by the former softening radius. Therefore, with the improved resolution, the central surface density increases as the gas reaches a new hydrostatic equilibrium closer to the MBH, as shown in Fig. 6 (red line). The lack of noticeable differences in the surface profile at separations R > 3 pc confirms the accuracy of the particle splitting technique.

Results of the high resolution run are shown in Fig. 7. The separation decays down to 0.1 pc in \sim 10 Myrs. We notice that the ellipsoidal torque regime, defined in Escala et al. 2004 (see also Escala et al. 2005) and characterized by a fast orbital decay, is not present. We attribute this difference to the different thermal state of the gas surrounding the MBHs. For a comparison, we rescale the results of our simulation to the parameters used in Escala et al. (2005). After rescaling, our initial disc is found to be hotter by a factor \approx 2.4 than the hottest disc model presented in Escala et al. (2005). Since the efficiency of angular momentum transport by ellipsoidal deformations decreases with increasing temperature, in our hotter disc dynamical friction driven torques still dominate over the ellipsoidal torques.

In the high resolution run, the dynamical evolution of the MBHs is initially identical to the low resolution case, as shown in Fig. 7. Because of particle splitting, the system

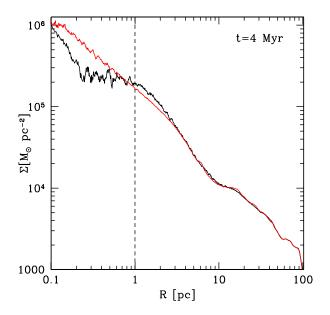


Figure 6. Surface density profile of the circum–nuclear gaseous disc in run A1 at t=4 Myrs. Black line refers to the surface density in the low resolution simulation, red line refers to the high resolution (split) simulation. The dashed vertical line marks the resolution limit in the un–split simulation.

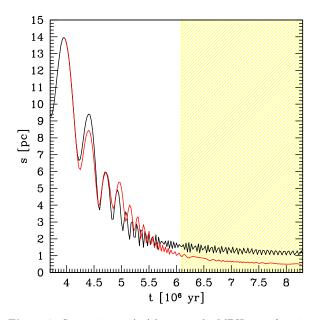


Figure 7. Separations s (pc) between the MBHs as a function of time. Red (black) line refers to the (un–)split run A1. The dashed area highlight when the MBHs separation is < 1 pc (corresponding to the low numerical resolution) in the split run A1.

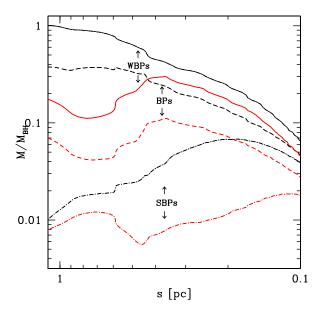


Figure 8. Mass of bound gas particles as a function of binary separation s in the final stages (from ≈ 6 to ≈ 8.5 Myrs) of the high resolution simulation (split run A1). Black lines refer to gas particles bound to the MBH initially at rest (primary), red lines refer to gas particles bound to the secondary MBH. Solid, dashed, and dot—dashed lines refer to WB, B, and SB particles.

granularity is reduced, and therefore the force resolution increases. In the high resolution run, the binary decreases its eccentricity to ≈ 0 (before the new spatial resolution limit is reached).

A resolution of 0.1 pc allows us to study the properties of the gas bound to each MBH. To this purpose, it is useful to divide gaseous particles, bound to each MBH, into three subsets, according to their total energy relative to the MBH. We then define weakly bound (WB), bound (B), and strongly bound (SB) particles according to the following rule:

$$E < \begin{cases} 0 & \text{(WB)} \\ 0.25 W & \text{(B)} \\ 0.5 W & \text{(SB)}, \end{cases}$$
 (5)

where E is the sum of the kinetic, internal and gravitational energy (per unit mass), the latter referred to the gravitational potential W of each individual MBH. Hereafter WBPs, BPs, and SBPs will denote particles satisfying the WB, B, or SB condition, respectively. Note that, with the above definition, SBPs are a subset of BPs, which in turn are a subset of WBPs.

We find that the mass collected by each MBH, relative to WB, B, and SB particles is $M_{\rm WBP}\approx 0.85 M_{\rm MBH}\approx 3.4\times 10^6 {\rm M}_{\odot},~M_{\rm BP}\approx 0.41 M_{\rm MBH}\approx 1.6\times 10^6 {\rm M}_{\odot},$ and $M_{\rm SBP}\approx 0.02 M_{\rm MBH}\approx 8\times 10^4 {\rm M}_{\odot},$ respectively (here $M_{\rm MBH}=M_1=M_2$ of run A1). These masses are of the same order for both the primary and secondary MBH, and remain constant as long as the MBH separation is $s\gtrsim 1$ pc. At shorter separations WBPs and BPs are perturbed by the tidal field of each MBH, and at the end of the simulation $M_{\rm WBP}$ and $M_{\rm BP}$ are reduced as shown in Fig.8. During

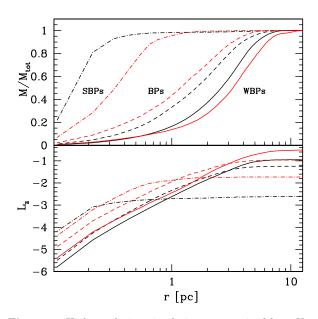


Figure 9. High–resolution simulation at t=4.5 Myrs. Upper panel: gaseous cumulative mass fraction of bound particles (for the SBPs, BPs, and WBPs, respectively) as a function of the distance from each MBH. Lower panel: z–component of cumulative orbital angular momentum, per unit bound mass, as a function of the distance from each MBH. Black (red) lines refer to the initial central primary (orbiting secondary) MBH. Solid, dashed, and dotted–dashed lines refer to WBPs, BPs, and SBPs, respectively.

the same period of time, $M_{\rm SBP}$ associated to the primary (secondary) MBH increases by a factor $\approx 4~(\approx 2.5)$. This result is unaffected by numerical noise since the number of bound particles (associated to each class) is $\gtrsim 1~\rm SPH$ kernel ($N_{\rm neigh}=50$).

The radial density profiles of WBPs, BPs, and SBPs are well resolved during the simulation. The upper panel of Fig. 9 shows the normalized mass within distance r from each MBH, for WBPs, BPs, and SBPs, at t = 4.5 Myrs, when the binary separation is ≈ 5 pc. The lower panel of Fig. 9 shows the specific angular momentum perpendicular to the disc plane (L_z) of the particles, computed in each MBH frame. Bound particles have a net angular momentum with respect to each MBH, and form a pressure supported ellipsoid. The half-mass radius is similar for the two MBHs: \simeq 3 pc, \simeq 1 pc, and \simeq 0.2 pc for WBPs, BPs, and SBPs, respectively. The disc gas density can be as high as 10^7 cm⁻³. It is then conceivable that, at these high densities, dissipative processes could be important, possibly reducing the gas internal (turbulent and thermal) energy well below the values adopted in our simulations. If any dissipative precess could reduce efficiently the gaseous internal energy, we expect that the bound gas will form a cool disc with Keplerian angular momentum comparable to what we found in our split simulation (see Fig. 9). Since $L_z = \sqrt{G M_{\text{MBH}} R_{\text{MBH,disc}}}$, we obtain, for the primary MBH, an effective radius $R_{\rm MBH, disc} \approx 0.1$ pc (0.03 pc) for WBPs (BPs). The secondary MBH is surrounded by particles with a comparatively higher angular momentum (see red lines in Fig. 9, lower panel), with a corresponding effective radius $R_{\rm MBH, disc} \approx 1$ (0.13) pc for WBPs (BPs). Finally, for SBPs, both holes have $R_{\rm MBH, disc} \ll 0.01$ pc, which is more than an order of magnitude below our best resolution limit. These simple considerations indicate that a more realistic treatment of gas thermodynamics is necessary to study the details of gas accretion onto the two MBHs during the formation of the binary, and the subsequent orbital decay. Nonetheless, our simplified treatment allows us to estimate a lower limit to the accretion timescale, assuming Eddington limited accretion:

$$t_{\rm acc} = \frac{\epsilon}{1 - \epsilon} \tau_{\rm Edd} \ln \left(1 + \frac{M_{\rm acc}}{M_{\rm MBH,0}} \right), \tag{6}$$

where ϵ is the radiative efficiency, $\tau_{\rm Edd}$ is the Salpeter time, $M_{\rm MBH,0}$ is the initial MBH mass, and $M_{\rm acc}$ is the accreted mass. Assuming $\epsilon=0.1$, Eddington limited accretion can last for ~ 30 Myrs, ~ 15 Myrs, and $\lesssim 1$ Myrs, if the MBHs accrete all the WBPs, BPs, and SBPs, respectively.

4 DISCUSSION

In this paper we have shown that dynamical friction against a gaseous and/or stellar background is responsible for the inspiral of MBH pairs inside massive nuclear discs. A MBH binary forms at a separation ~ 5 pc. The density and thermal distributions of the gas and star particles around the binary MBH are such that dynamical friction keeps acting on each MBH down to a separation of ≈ 1 pc since the coherence of the density wakes excited by the MBHs is maintained down to this scale. Thanks to the particle splitting technique applied to the case of a purely gaseous disc, we follow the binary orbital decay down to ≈ 0.1 pc, and we show that angular momentum losses by friction, along co–rotating orbits, reduce the orbital eccentricity to a value consistent with zero.

Other processes neglected in our study can help to shrink the binary orbit. For example, three—body encounters with background stars may become important at MBHs separations $\lesssim r_{\rm inf} \approx 6$ pc (Quinlan 1996; Milosavljevic & Merritt 2001; Merritt 2006). The cumulative effect of this collisional process, studied mainly in spherical backgrounds, can lead to an increase of the eccentricity, thus acting against the circularization driven by the large—scale action of the gaseous and/or stellar disc (Quinlan 1996; Aarseth 2003; Matsubayashi, Makino & Ebisuzaki 2005; Berczik et al. 2006; Sesana et al. in preparation). The effect of three body encounters on the MBH orbits when stars form a rotationally supported disc is still unclear.

We also quantified the structure of gas particles which become bound to each MBH during the orbital evolution. We found that during the orbital inspiral, a gas mass $\simeq 50\%$ of the MBH mass is conveyed inside the MBH sphere of influence, and that a gas mass $\approx 2\%$ of the MBH mass binds deeply to each single MBH. The radial distribution of the most bound gas particles suggests that an active Eddington–limited accretion phase may set in, for a time $\lesssim 1$ Myrs around both MBHs. Since we have neglected gas cooling in the simulation, this mass likely represents a lower limit. The active phase could last for a longer time ($\gtrsim 10$ Myrs), comparable to the inspiral timescale, if all the bound mass is

accreted. This highlights the possibility of revealing double AGN activity, on spatial scales $s \lesssim 10$ pc. However, since we expect that star formation is still ongoing in the disc while the MBHs spiral in, double AGN activity could be heavily obscured. In the same high resolution simulation, we measured the cumulative angular momentum (perpendicular to the disc) of particles bound to each individual MBH, allowing an estimate of the size of the Keplerian disc that is expected to form. We found disc sizes of ≈ 0.1 pc and $\ll 0.01$ pc for the bound and the strongly bound gas components, respectively. Such small extension of the accretion disc around each MBH could preserve the gas against tidal perturbation and stripping, at least until the binary reaches separations of the same order.

We plan to carry on higher resolution simulations with more realistic input physics and radiative cooling, in order to follow the last phases of the gas–dynamical evolution of the nuclear discs. In particular, we aim at tracing the expected transition of the two discs into a single, circumbinary disc surrounding the two MBHs.

Armitage & Natarajan (2002) have shown that the interaction between the two MBHs and the circumbinary disc can drive the binary to coalescence in ~ 10 Myrs, for MBH separations $\lesssim 0.1$ pc. They have also shown that, during the process, the MBH binary orbital eccentricity increases (Armitage & Natarajan 2005). Our planned future simulations will test in a self–consistent way such predictions, and will explore the possibility of exciting flaring activity during the latest phases of MBH binary inspiral. This will constrain the properties of an electromagnetic precursor associated to the binary coalescence (Armitage & Natarajan 2002; Kocsis et al. 2005; Milosavljevic & Phinney 2005; Dotti et al. 2006).

ACKNOWLEDGMENTS

REFERENCES

Arena S.E., Bertin G., 2007, A&A 463, 921

Armitage P.J., Natarajan P., 2002, ApJ, 567, L9

Armitage P.J., Natarajan P., 2005, ApJ, 634, 921

Aarseth S. J., 2003, Ap&SS, 285, 367

Barnes J. E., Hernquist L., 1991, ApJ, 370, L65

Barnes J. E., Hernquist L., 1996, ApJ, 471, 115

Bate M. R., Burkert A., 1997, MNRAS, 288, 1060

Bender P. et al. 1994, LISA, Laser Interferometer Space Antenna for gravitational wave mesuraments: ESA Assessment Study Report

Berczik P., Merritt D., Spurzem R., Bischof H.P., 2006, ApJ, 642, 21

Brown W.R., Geller M.J., Kenyon S.J., Kurtz M.J., 2006, ApJ, 647, 303

Bryant P.M., Scoville N. Z., 1999, AJ, 117, 263

Colpi M., Mayer L., Governato F., 1999, ApJ, 525, 720

Davies R., Mueller Sanchez F., Genzel R., Tacconi L., Hicks E., Friedrich S., Sternberg A. submitted to ApJ (arXiv:0704.1374)

Dotti M., Colpi M., Haardt F., 2006, MNRAS, 367, 103 (DCH2006)

Dotti M., Salvaterra R., Sesana A., Colpi M., Haardt F., 2006, MNRAS, tmp 997D

Downes D., Solomon P.M., 1998, ApJ, 507, 615

Escala A., Larson R.B., Coppi P.S., Maradones D., 2004, ApJ, $607,\,765$

Escala A., Larson R.B., Coppi P.S., Maradones D., 2005, ApJ, $630,\,152$

Ferrarese L., et al., 2006, ApJS, 164, 334

Greve T.R., Papadopoilos P.P., Gao Y., Radford S.J.E., 2006, submitted to ApJ (astro-ph/0610378)

Hughes S. A., 2002, MNRAS, 331, 805

Kazantzidis S. et al., 2005, ApJ, 623, L67

Kitsionas S., Whitworth S., 2002, MNRAS, 330 129

Kocsis B., Frei Z., Haiman Z., Menou K., 2005, ApJ, 637, 27

Komossa S., Burwitz V., Hasinger G., Predehl P., Kaastra J.S., Ikebe Y., 2003, ApJ, 582, L15

Komossa S., 2006, Mem. Soc. Astron. Ital., 77, 733

Kormendy J., Gebhardt K., Fisher D.B., Drory N., Macchetto F.D., Sparks W.B., 2005, AJ, 129, 2636

Krajnovic D., Jaffe W., 2004, A&A, 428, 887

Lopes R.D.S., Storchi-Bergmann T., Saraiva M.F.O., Martini P., ApJ in press (astro-ph/0610380)

Mayer L., Kazantzidis S., Madau P., Colpi M., Quinn T., Wadsley J., 2006, to appear in the Proceedings of the Conference "Relativistic Astrophysics and Cosmology - Einstein's Legacy" (astro-ph/0602029)

Matsubayashi T., Makino J., Ebisuzaki T., 2005, preprint astro-ph/0511782

Merritt D., 2006, ApJ, 648, 976

Milosavljevic M., Merritt D., 2001, ApJ, 563, 34

Milosavljevic M., Merritt D., Armin R., van den Bosch F.C., 2002, MNRAS, 331, 51

Milosavljevic M., Phinney E. S., 2005, ApJ, 622, L93

Morelli L., et al., 2004, MNRAS, 354, 753

Mueller Sanchez F., Davies R., Eisenhauer F., Tacconi L., Genzel R., Sternberg A., 2006, A&A, 454, 481

Ostriker E., 1999, ApJ, 513,252

Quinlan G. D., 1996, NewA, 1, 35

Risaliti G., et al., 2006, ApJ, 637, L17

Sanchez-Salcedo F.J., Brandenburg A., 2001, MNRAS, 322, 67

Sanders D.B., Mirabel I.F., 1996, ARA&A, 34, 749

Scoville N.Z., Yun M.S., Bryant P.M., 1997, ApJ, 484, 702

Scorza C., van den Bosch F.C., 1998, MNRAS, 300, 469

Sesana A., Haardt F., Madau P., Volonteri M., 2005, ApJ, 623, 23

Springel V., Yoshida N., White S.D.M., 2001, NewA, 6, 79

Tacconi L.J., Genzel R., Tecza M., Gallimore J.F., Downes D., Scoville N.Z., 1999, ApJ, 524, 732

van den Bosch F.C., Lewis G.F., Lake G., Stadel J., 1999, ApJ, 515, 50

van den Bosch F.C., Jaffe W., van der Marel R.P., 1998, MNRAS, 293. 343

Yu Q., Tremaine S., 2003, ApJ, 599, 1129